Finite Volume Particle Method for 3-D Elasto-Plastic Solid Simulation

Ebrahim Jahanbakhsh, Christian Vessaz, François Avellan
Laboratory for Hydraulic Machines
École polytechnic fédérale de Lausanne (EPFL)
Lausanne, Switzerland
ebrahim.jahanbakhsh@epfl.ch, christian.vessaz@epfl.ch, francois.avellan@epfl.ch

***Abstract*—Finite Volume Particle Method was successfully used to predict fluid flow behavior for 2-D simulations. In this paper, we present a FVPM which is applicable for 3-D solid mechanics simulations. This method features rectangular top-hat kernels for computing the interaction vectors exactly and efficiently. We employed this method to solve the elasto-plastic constitutive equations. To validate the model, we study the impact of rigid spherical particle to the solid surface with different velocities and compare the residual stress and plastic deformation with the FEM solutions.**

I. Introduction

Fluid flow advecting silts originating from snow, glaciers or monsoons can cause severe erosion when passing through the turbines. Erosive wear occurs when silt particles collide into the material and remove part of it due to the repeated plastic deformations. The purpose of this paper is to present a particle-based method, which is capable to predict the plastic behavior of the material under the silt impact loads.

The Finite Volume Particle Method (FVPM) is a particle-based method introduced by Hietel [1]. This method includes many of the desirable features of mesh-based finite volume methods. FVPM profits from particle interaction vectors to weight conservative fluxes exchanged between particles. In this methods, computational nodes are usually moving with material velocity which is compatible with the Lagrangian form of the motion equations. FVPM has some features of SPH but unlike SPH, it is locally conservative regardless of any variation in particle smoothing length. This enables the users to refine the solution by splitting particles into smaller ones in the region of interest and perform the simulation efficiently. Recently, Quinlan and Nestor [2] proposed a method to compute the interaction vectors for 2-D cases exactly. Following their work, Jahanbakhsh [3] developed an exact FVPM applicable for 3-D cases. This method features the rectangular top-hat kernel and is implemented in SPHEROS software [4].

In the present paper, we discretize the elasto-plastic constitutive equations based on the mentioned 3-D FVPM. To validate the model, we select a problem concerning the shot impact to the solid material. This test case is selected due to its close relation to erosive wear mechanism. The numerical study is performed for normal impact of a single shot to the solid plate. We study the effect of two impact velocities of 75 and 100 m s^{-1}. We validate the method by comparing the residual stress and plastic deformation with the FEM solutions of Meguid et al. [5] and Hong et al. [6].

The structure of the paper is as following. In the next section, we present the governing equations including constitutive model for solid, silt motion and the contact force. Then, FVPM with rectangular top-hat kernel discretization is presented. Later, the strategy used for particle splitting is explained. We present the solution algorithm and numerical results afterward.

II. Governing Equations

A. Solid state

The solid motion is governed by mass and linear momentum conservation equations as

$$\frac{d\rho}{dt} = -\rho \nabla \cdot \mathbf{C} \tag{1}$$

$$\frac{d\left(\rho \mathbf{C}\right)}{dt} = \nabla \cdot \boldsymbol{\sigma} + \mathbf{f}_c + \rho \mathbf{g} \tag{2}$$

where $\frac{d}{dt}$ denotes substantial derivative, ρ is the density, $\mathbf{C}$ is the velocity vector, $\mathbf{g}$ is the gravitational acceleration and $\boldsymbol{\sigma}$ is the Cauchy's stress tensor. To model the effect of silt, the contact force, $\mathbf{f}_c$, exerted by silt particles in considered in linear momentum equation.

The Cauchy's stress tensor, $\boldsymbol{\sigma}$, is decomposed as

$$\boldsymbol{\sigma} = \mathbf{s} - p\mathbf{I} \tag{3}$$

where $\mathbf{s}$ represents the deviatoric stress tensor and p represents the pressure obtained from equation of state

$$p = a^2\left(\rho - \rho_\circ\right) \tag{4}$$

In (4), a and $\rho_\circ$ denote to the sound speed and reference density respectively. For a given bulk modulus, K, the sound speed is computed as

$$a = \sqrt{\frac{K}{\rho}} \tag{5}$$

The rate of deviatoric stress, $\dot{\mathbf{s}}$, is described by the Jaumann rate of stress, $\mathbf{s}^\nabla$, as

$$\mathbf{s}^\nabla = \dot{\mathbf{s}} - \mathbf{s}\cdot\boldsymbol{\Omega} - \boldsymbol{\Omega}\cdot\mathbf{s} \tag{6}$$

where $\mathbf{\Omega}$ is rotation tensor

$$\mathbf{\Omega} = \frac{\nabla \mathbf{C} - (\nabla \mathbf{C})^T}{2} \tag{7}$$

For small deformations, the strain rate tensor, $\dot{\mathbf{e}}$, is linearized and approximated as

$$\dot{\mathbf{e}} \approx \dot{\boldsymbol{\varepsilon}} = \mathbf{D} = \frac{\nabla \mathbf{C} + (\nabla \mathbf{C})^T}{2} \tag{8}$$

and the deviatoric strain rate tensor, $\dot{\boldsymbol{\varepsilon}}'$, is found by

$$\dot{\boldsymbol{\varepsilon}}' = \dot{\boldsymbol{\varepsilon}} - \frac{1}{3}\mathrm{tr}\left(\dot{\boldsymbol{\varepsilon}}\right)\mathbf{I} \tag{9}$$

According to Hooke's law, with shear modulus G we could write

$$\mathbf{s}^{\nabla} = 2G\dot{\boldsymbol{\varepsilon}}' \tag{10}$$

Substituting (10) into (6) and integrating in time yields

$$\mathbf{s}^{(*)} = \mathbf{s}^{(t)} + \left(\mathbf{s}\cdot\mathbf{\Omega} + \mathbf{\Omega}\cdot\mathbf{s} + 2G\dot{\boldsymbol{\varepsilon}}'\right)\Delta t \tag{11}$$

where $\mathbf{s}^{(*)}$ denotes to the trial stress tensor. The effective trial stress is defined by

$$s^{(*)} = \sqrt{\frac{3}{2}\mathbf{s}^{(*)} : \mathbf{s}^{(*)}} \tag{12}$$

In present study, we assume solid as an isotropic elasto-plastic material. The constitutive model is based on radial return plasticity explained in [7]. If $s^{(*)}$ exceeds yield stress, σ_y, the Von Mises flow rule

$$f\left(\boldsymbol{\sigma}, \varepsilon_p\right) = \sqrt{\frac{3}{2}\mathbf{s} : \mathbf{s}} - \sigma_y\left(\varepsilon_p\right) \leq 0 \tag{13}$$

is violated and we scale the trial stresses back to the yield surface

$$\mathbf{s}^{(t+\Delta t)} = m\mathbf{s}^{(*)} \tag{14}$$

where $m = \frac{\sigma_y^{(t+\Delta t)}}{s^{(*)}}$ is called radial return factor.

For isotropic linear strain hardening models, the yield stress is evolved by

$$\sigma_y^{(t+\Delta t)} = \sigma_y^{(t)} + E^p \Delta\varepsilon_p \tag{15}$$

where $\Delta\varepsilon_p$ denotes to the effective plastic strain increment

$$\Delta\varepsilon_p = \sqrt{\frac{2}{3}\Delta\boldsymbol{\varepsilon}_p : \Delta\boldsymbol{\varepsilon}_p} \tag{16}$$

After some mathematical operations, see [7], the effective plastic strain increment reads

$$\Delta\varepsilon_p = \frac{s^{(*)} - \sigma_y^{(t)}}{3G + E^p} \tag{17}$$

According to [8], the dissipated energy due to the plastic deformation is

$$W_p = \int_0^t \int_{\Omega(\tau)} \boldsymbol{\sigma} : \dot{\boldsymbol{\varepsilon}}_p dV d\tau \tag{18}$$

We define dissipated energy density, w_p, as

$$w_p = \int_0^t \boldsymbol{\sigma} : \dot{\boldsymbol{\varepsilon}}_p d\tau \tag{19}$$

Neglecting the volumetric plastic strains, the increment for dissipated energy density is approximated by

$$\Delta w_p = \boldsymbol{\sigma}^{(t+\Delta t)} : \Delta\boldsymbol{\varepsilon}_p = \mathbf{s}^{(t+\Delta t)} : \Delta\boldsymbol{\varepsilon}_p \tag{20}$$

Finally, Δw_p is computed as

$$\Delta w_p = \Delta\varepsilon_p\left(ms^{(*)}\right) = \Delta\varepsilon_p\sigma_y^{(t+\Delta t)} \tag{21}$$

The deviatoric stress, plastic strain, and dissipated energy density is computed and stored at the midpoint of two interacting particles. Therefore, the velocity gradient is needed there. Nestor et al. [9] used a re-normalized SPH operator to compute the the velocity gradient at the midpoint. Here, we use the weighted least squares approach to compute the gradients [3]. Thus, for particles i and j, the deformation rate and rotation tensors is computed as

$$\mathbf{D}_{ij} = \frac{1}{2}\left(\tilde{\nabla}\mathbf{C}_{ij} + \left(\tilde{\nabla}\mathbf{C}_{ij}\right)^{\mathrm{T}}\right) \tag{22}$$

$$\mathbf{\Omega}_{ij} = \frac{1}{2}\left(\tilde{\nabla}\mathbf{C}_{ij} - \left(\tilde{\nabla}\mathbf{C}_{ij}\right)^{\mathrm{T}}\right) \tag{23}$$

where $\tilde{\nabla}$ denotes to the gradient operator obtained from weighted least squares. This way, we avoid double summation gradient operators and accordingly a more compact computational stencil is obtained.

B. Rigid Silt Particle and Contact Modeling

Silt particles are assumed rigid and spherical. Hence, their mass and volume remains constant and their acceleration is found from Newton's second law

$$m\frac{d\mathbf{C}}{dt} = \mathbf{f}^c + m\mathbf{g} \tag{24}$$

where m denotes to the silt mass and $\mathbf{f}^c$ is the contact force exerted from solid.

To evaluate the contact force, we assume that the solid particles are spheres with radii of h, see Fig. (1). Doing this, the contact force $\mathbf{f}^c$ is computed as penalty force. Each particle is checked for penetration through the other particle surface. If the particles penetrate, a penalty force in direction of centers is applied between the particles at their contact point. The magnitude of this force is proportional to the amount of penetration and is computed according to Hertz contact theory. For contact between two spheres of radii R_1 and R_2, the contact force vector is given by

$$\mathbf{f}^c = \left(\frac{4E}{3}R^{\frac{1}{2}}d^{\frac{3}{2}}\right)\mathbf{e} \tag{25}$$

where, $\mathbf{e}$ denotes to the unit vector passing through the particle centers and d is the penetration depth. R and E are the effective radius and Young modulus respectively defined as

$$\frac{1}{R} = \frac{1}{R_1} + \frac{1}{R_2} \tag{26}$$

$$\frac{1}{E} = \frac{1-\nu_1^2}{E_1} + \frac{1-\nu_2^2}{E_2} \tag{27}$$

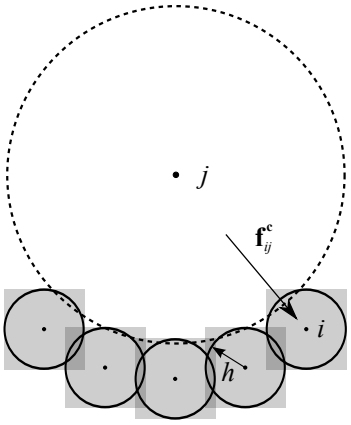

Fig. 1: Interaction of silt and solid particles is accomplished by contact force. The dashed line indicates the boundary of silt particle j. The solid particles are assumed as circles with radii h. The contact force $\mathbf{f}_{ij}^{c}$ is computed for particle i in direction of center lines

where E_1, E_2 are the Young modulus and ν_1, ν_2 the Poisson's ratios associated with each particle. It is worth to note that, for the rigid silt particle, the Young modulus is infinity. Therefore, its effect would be canceled from (27).

III. FVPM

In FVPM, the Sheppard function is used as the interpolating or shape function. Sheppard interpolation is equivalent to Moving Least Squares (MLS) interpolating function with zero-order basis [10]. Shepard function $\psi_i(\mathbf{x})$ for a given point i reads

$$\psi_i(\mathbf{x}) = \frac{W_i(\mathbf{x})}{\sigma(\mathbf{x})} \tag{28}$$

where $W_i(\mathbf{x}) = W_i(\mathbf{x} - \mathbf{x}_i, h_i)$ is the kernel function and σ is the kernels summation. h_i is the smoothing length at the given point and represents the spatial resolution of the interpolation. Sheppard interpolation is zero-order consistent which means that a constant function could be reproduced exactly. These shape functions are used in discretization of the PDE arising from the conservation law

$$\frac{\partial \mathbf{U}}{\partial t} + \nabla \cdot \mathbf{F}(\mathbf{U}) = 0 \tag{29}$$

where $\mathbf{U}$ is the conserved variables and $\mathbf{F}$ represents the flux functions. For solid equation, $\mathbf{U}$ and $\mathbf{F}$ are equal to $\{\rho, \rho\mathbf{C}\}$ and $\{\rho\mathbf{C}, \rho\mathbf{C}\mathbf{C} - \boldsymbol{\sigma}\}$ respectively. According to [3], we write the discretized equations in locally conservative form as

$$\frac{d}{dt}(\mathbf{U}_i V_i) + \sum_j \mathbf{U}_{ij}(\dot{\mathbf{x}}_i \cdot \boldsymbol{\Gamma}_{ji} - \dot{\mathbf{x}}_j \cdot \boldsymbol{\Gamma}_{ij}) + \sum_j \mathbf{F}_{ij} \cdot \boldsymbol{\Delta}_{ij} = 0 \tag{30}$$

where V_i is particle volume and $\dot{\mathbf{x}}_i$ denotes to the particle velocity. In present study, $\dot{\mathbf{x}}_i$ is always equal to material velocity $\mathbf{C}_i$. $\boldsymbol{\Gamma}_{ij}$ and $\boldsymbol{\Delta}_{ij}$ are defined as

$$\boldsymbol{\Gamma}_{ij} = \int_\Omega \frac{W_i \nabla W_j}{\sigma^2} dV \tag{31}$$

$$\boldsymbol{\Delta}_{ij} = \boldsymbol{\Gamma}_{ij} - \boldsymbol{\Gamma}_{ji} \tag{32}$$

$\mathbf{U}_{ij}$ is found by averaging the conserved variables of particles i and j. The $\mathbf{F}_{ij}$ consists of deviatoric stress, pressure and invicid flux $\rho\mathbf{C}\mathbf{C}$. Deviatoric stress is updated according to the method described in section II-A. For the pressure and invicid flux we use the average of particle's values. We add artificial viscosity Π_{ij} into the momentum flux to avoid nonphysical oscillations. The Π_{ij} is computed as proposed by Monaghan [11].

The particle volume is evolved by

$$\frac{dV_i}{dt} = \sum_j (\dot{\mathbf{x}}_j \cdot \boldsymbol{\Gamma}_{ij} - \dot{\mathbf{x}}_i \cdot \boldsymbol{\Gamma}_{ji}) + \dot{\mathbf{x}}_i \cdot \mathbf{S}_i \tag{33}$$

where $\mathbf{S}_i = \sum_j \boldsymbol{\Delta}_{ij}$. The term $\dot{\mathbf{x}}_i \cdot \mathbf{S}_i$ in (33) is included to satisfy the free surface boundary condition [3]. As discussed by Quinlan and Nestor [2], considering the exact integration of interaction vectors, the $\mathbf{S}_i$ vanishes for the interior particles.

IV. Rectangular Top-hat Kernel

In present study, we use rectangular kernels to compute the particle interaction vectors in 3-D case. To compute these vectors, the integral defined in (31) has to be evaluated. For conventional bell-shaped kernels, this integral is difficult or impossible to be evaluated exactly. The alternative approach is to use the Quadrature rules which become very costly in 3-D. Recently, Quinlan and Nestor [2] used 2-D top-hat kernel with circular support, which enables them to compute the integrals exactly and efficiently. Implementing the spherical support kernels for 3-D case requires huge geometric computations which again increases the computational cost. Here, we use top-hat kernel but instead of spherical support, we consider rectangular support kernel for the particles. Using rectangular support kernels induces less geometric computations and yields to an efficient and exact method for 3-D cases.

The rectangular top-hat kernel is defined as

$$W_i(\mathbf{x}) = \begin{cases} 1 & \|\mathbf{x} - \mathbf{x}_i\|_\infty \leq h_i \\ 0 & \|\mathbf{x} - \mathbf{x}_i\|_\infty > h_i \end{cases} \tag{34}$$

Fig. 2(a) shows a system of particles and their overlapping regions with rectangular support kernels in 2-D. The Sheppard shape function contours corresponding to particle i are shown in Fig. 2(b) and 2(c) for bell-shaped and top-hat kernels respectively. It is visible that bell-shaped kernel results in a smoother shape function.

According to (34), ∇W is zero everywhere and is not defined at the particle smoothing border. However, the integral corresponding to the interaction vector $\boldsymbol{\Gamma}_{ij}$ is defined. After some mathematical operations [3], the integral in (31) is simplified as

$$\boldsymbol{\Gamma}_{ij} = -\sum_l^m \left(\frac{\Delta \mathbf{S}_l}{\sigma_l^+ \sigma_l^-} \right) \tag{35}$$

According to (35), the surface corresponding to the intersection of particles i and j is partitioned to m rectangles. These partitioning is due to other particles intersections. In (35), $\Delta\mathbf{S}$

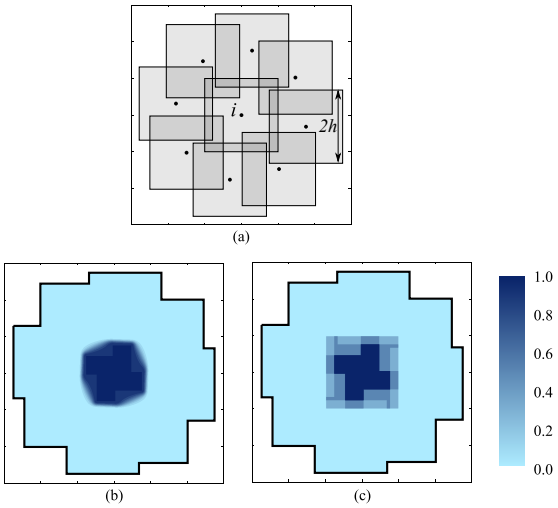

Fig. 2: Rectangular support kernels and overlapping regions indicated in shaded areas (a). Contours of Sheppard shape function corresponding to particle i is plotted for (b) bell-shaped kernel and (c) top-hat kernel.

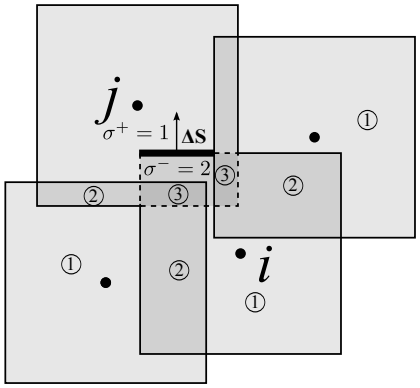

Fig. 3: Intersection volume of particles i and j is indicated by dashed line. It splits to different segments. σ^+ ,σ^- and area vector $\Delta\mathbf{S}$ are shown for the thick segment. The numbers inside the circle denotes to σ.

denotes to the surface vector of partitions, σ^+ is the summation of the kernels outside of the intersection zone and σ^- is the summation of the kernels which appear at the surface. A 2-D representation of the partitioning is shown in Fig. 3. The rectangular partitions are simplified to line segments for 2-D case.

V. Particle Splitting

FVPM formulation enables to handle different size or smoothing length of particles. Here, we refine the solution by splitting the particles which are near the contact point. This procedure is performed in two steps. First, the original particle is split into eight fine particles and secondly, the field variables are mapped from the original particles to the split ones. After splitting, the volume of fine particles are computed as

$$V_i = \sum_j V_{ij} \tag{36}$$

where V_{ij} is computed by

$$V_{ij} = \int_\Omega \psi_i \psi_j dV \tag{37}$$

For the field variables like pressure, stress, density and velocity, we use the original particle's value. The mass of refined particles is found from the density and volume as

$$m_i = \rho_i V_i \tag{38}$$

The split particles are distributed within the smoothing volume of the original one. The union of the smoothing volume for the split particles has to be equal to the original smoothing volume. Hence, the smoothing length for split particles are depending on their position. We define η parameter which links the particle spacing δ to the smoothing length as

$$\eta = \frac{h}{\delta} \tag{39}$$

As it is visible in Fig. 4a, η value should be greater than 0.5 to generate the particle overlapping zones. On the other hand, the large values of η generates huge computational stencils and increases the computational cost. To our experiments, a reasonable value for η could be selected between 0.55 to 0.95. To distribute the particles, we change the η in a way that the successive splitting makes a pattern similar to mesh obtained by Adaptive Mesh Refinement technique [12]. For instance in 2-D case, the two particles shown in upper side of Fig. 4a, are split into four small ones shown in Fig. 4b. This distribution dictates the smoothing length for small particles as

$$\frac{h'}{h} = 1 - \frac{1}{4\eta} \tag{40}$$

where h' denotes to the split particle smoothing length. Finally, the η for r-times split particle reads

$$\eta^{(r)} = 2^r \left(\eta^{(0)} - \frac{1}{2}\right) + \frac{1}{2} \tag{41}$$

Equation (41) is valid for both 2-D and 3-D cases. In present study, we set the $\eta^{(0)}$ in such a way that the finest η is equal to 0.75.

VI. Solution Algorithm

We used second-order explicit Runge-Kuta scheme for the time integration. In this scheme, the conserved variables are updated for the half of the time step using the current time step values

$$\mathbf{U}^{(t+\frac{\Delta t}{2})} = \mathbf{U}^{(t)} - \nabla \cdot \mathbf{F}\left(\mathbf{U}^{(t)}\right)\frac{\Delta t}{2} \tag{42}$$

Then, the intermediate fluxes are computed using the half time step values. And finally, the conserved variables for new time step is found by

$$\mathbf{U}^{(t+\Delta t)} = \mathbf{U}^{(t)} - \nabla \cdot \mathbf{F}\left(\mathbf{U}^{(t+\frac{\Delta t}{2})}\right)\Delta t \tag{43}$$

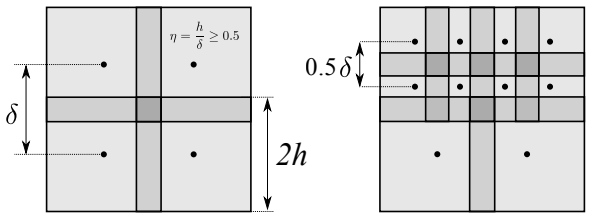

Fig. 4: Schematic diagram of particle splitting in 2-D case. (a) The original particle distribution and (b) The split particle distribution

The stress tensor and plastic strain are updated according to forward Euler time integration scheme. The solution algorithm is shown in Algorithm 1. For a given CFL number, the Δt is adapted for each step as

$$\Delta t = \text{CFL} \times \min\left(\frac{h_i}{a + |\mathbf{C}_i|}\right) \tag{44}$$

VII. Results

To validate the code for plastic deformation, we simulated a test case concerning the shot-peening process. In shot-peening process, the surface of metal is bombarded with spherical shots. Each shot impacting the surface, makes a tiny plastic deformation on it and produce a hemisphere zone with residual compressive stress. Overlapping these zones, forms a uniform layer stressed in compression underneath the metal surface. Here, we simulate a single shot impact and compare the residual stress distribution by FEM studies [5] and [6]. The case is set up according to Mequid et al. [5] FEM model. The problem dimensions and material properties are summarized as below, see Fig. 5.

- Solid dimensions are $W = 0.0035$ m, $H = 0.002$ m and $B = 0.0025$ m.
- Diameter of silt particle is $d = 0.001$ m.
- Silt and solid density is $\rho = 7800$ kg m^3.
- Initial yield stress for solid is $\sigma_y^0 = 6 \times 10^8$ Pa.
- Linear strain-hardening parameter for solid is $E^p = 8 \times 10^8$ Pa.
- Elastic modulus for solid is $E = 2 \times 10^{11}$ Pa.

The solid sample is fixed at the bottom. We enforce this condition by setting the velocity of the particles placed at the bottom to zero. The simulation has been performed for two different shot velocities of $\mathbf{C} = (-75, 0, 0)$ and $\mathbf{C} = (-100, 0, 0)$ m s^{-1}. To study the convergence of the method, each simulation is repeated for five different particle spacing of $\delta = \frac{d}{2}$, $\delta = \frac{d}{4}$, $\delta = \frac{d}{8}$, $\delta = \frac{d}{16}$ and $\delta = \frac{d}{32}$. The results has been achieved by splitting particles near the contact zone. For all the cases, the time steps is adapted to respect CFL$= 0.8$ and the simulation is run for 1×10^{-5} s. The artificial viscosity parameters α and β appears in Monaghan [11], is set to 0.2 and 0.4 respectively.

Algorithm 1 Solution algorithm

for each time step Δt **do**
  compute contact force from (25)
  compute $\frac{d}{dt}(m_i \mathbf{C}_i)$ for particle i
    if $(i \in \text{solid})$ **then** use (30)
    if $(i \in \text{silt})$ **then** use (24)
  compute $\frac{dm}{dt}$ for solid particle from (30)
  compute $\frac{dV}{dt}$ for solid particle from (33)
  update momentum and mass from (42)
  update volume $V_i^{(t+\frac{\Delta t}{2})} = V_i^{(t)} + \frac{dV}{dt}\frac{\Delta t}{2}$
  update density $\rho_i = \frac{m_i}{V_i}$
  compute pressure from equation of state (4)
  update particle velocity $\dot{\mathbf{x}}_i^{(t+\frac{\Delta t}{2})} = \mathbf{C}_i^{(t+\frac{\Delta t}{2})}$
  update deviatoric stress for particles i and j (11)
    if $s_{ij}^{(*)} > \sigma_y^{(t)}$, **then**
      solve for the plastic strain increment, (17)
      solve for the dissipated energy density, (21)
      update ε_p and w_p
      update yield stress (15)
      return deviatoric stress to yield surface (14)
    else
      $\mathbf{s}_{ij}^{(t+\Delta t)} = \mathbf{s}_{ij}^{(*)}$
  communicate variables
  compute contact force from (25)
  compute $\frac{d}{dt}(m_i \mathbf{C}_i)$, $\frac{dm}{dt}$ and $\frac{dV}{dt}$ for $(t + \frac{\Delta t}{2})$
  update momentum and mass from (43)
  update volume $V_i^{(t+\Delta t)} = V_i^{(t)} + \frac{dV}{dt}\Delta t$
  update density $\rho_i = \frac{m_i}{V_i}$
  compute pressure from equation of state (4)
  update particle velocity $\dot{\mathbf{x}}_i^{(t+\Delta t)} = \mathbf{C}_i^{(t+\Delta t)}$
  update position $\mathbf{x}_i^{(t+\Delta t)} = \mathbf{x}_i^{(t)} + \dot{\mathbf{x}}_i^{(t+\Delta t)}\Delta t$
  split particles
  search for neighboring particles
  communicate variables
  $t \leftarrow t + \Delta t$;
end for

Results shown in Fig. 6 are corresponding to the case of $|\mathbf{C}| = 75$ m s^{-1}. Fig. 6a depicts the time history of total dissipated plastic energy, W_p, normalized by initial kinetic energy of the shot which is the total energy of the system E_{total}. The total dissipated plastic energy is found by summation of the dissipated plastic energy for all solid particles as

$$W_p = \sum_i w_{pi} V_i \tag{45}$$

where w_{pi} denotes to the dissipated energy density for particle i. w_{pi} is the average of the midpoint values computed from (21). As it is visible, the dissipated plastic energy for particle spacing $\delta = \frac{d}{2}$ is too small. By reducing the particle spacing, this value converges to 90% of the E_{total}. The contribution of kinetic energy and plastic dissipated energy for different particle spacing is plotted in Fig. 6b. The kinetic energy shown, represent the shot particles kinetic energy after rebound. The

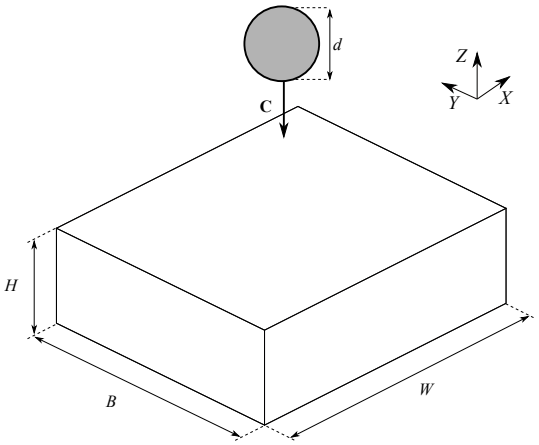

Fig. 5: Outline of single shot impact test case

kinetic energy of solid is negligible. The remaining energy is stored as elastic potential or dissipated due to the effect of artificial viscosity and numerical dissipation induced by spatial and temporal discretization. This effect is reduced for smaller particle spacing and converges to 5% of the E_{total}.

Fig. 6c shows the variation of residual stress σ_{xx} with depth along the central axis for different particle spacing. It is visible that the results are converging to the finest solution i.e. $\delta = \frac{d}{32}$. In Fig. 6d, the residual stress σ_{xx} obtained by FVPM is compared with Meguid et al. [5] and Hong et al. [6] results. As it is visible, there is a close match between the three sets of numerical results.

Fig. 7 shows the data for the case with $|\mathbf{C}| = 100$ m s^{-1}. Similar to previous case, the time history for total dissipated plastic energy is shown in Fig. 6a and the results are converging to 86% of the E_{total}. The contribution of kinetic and dissipated energy is depicted in 6b. For this case, 10% of the E_{total} is stored as elastic potential energy or dissipated by artificial viscosity and numerical dissipation. In Fig. 7c the residual stress σ_{xx} for different particle spacing are plotted which converges to the finest solution i.e. $\delta = \frac{d}{32}$. The σ_{xx} corresponding to the $\delta = \frac{d}{32}$ is compared with Meguid et al. [5] and Hong et al. [6] results in Fig. 7d. A good agreement is observed between FVPM and other numerical results.

Snapshots of the case $|\mathbf{C}| = 75$ m s^{-1} with $\delta = \frac{d}{32}$ after shot impact are shown in Fig. 8. In Fig. 8a, the residual stress contours in XZ plane is plotted and compared with Meguid et al. [5] results. The plastic deformation made by shot impact is also visible. It shows a good agreement with Meguid et al. [5] solution. In Fig. 8b, a 3-D view of solid colored by σ_{xx} is shown. Here, the solid particles are represented by spheres with radius equal to h. Particles near the contact point has been split for five level from $\delta_0 = d$ to $\delta = \frac{d}{32}$ which results in a refined solution.

VIII. Conclusion

We presented a 3-D FVPM method. This method features rectangular top-hat kernel which enables us to integrate the interaction vectors exactly and efficiently. This method is employed to discretize the solid motion equation with elasto-plastic constitutive model. We also presented a contact model to evaluate the contact force applied between rigid spherical particle and solid. We introduced a splitting method which preserve the computational volume of original particles. We simulated the case of single shot impact to the solid surface. We studied the convergence of the method for two different velocity of shot. Finally, we compared our results with FEM solutions which showed a good agreement.

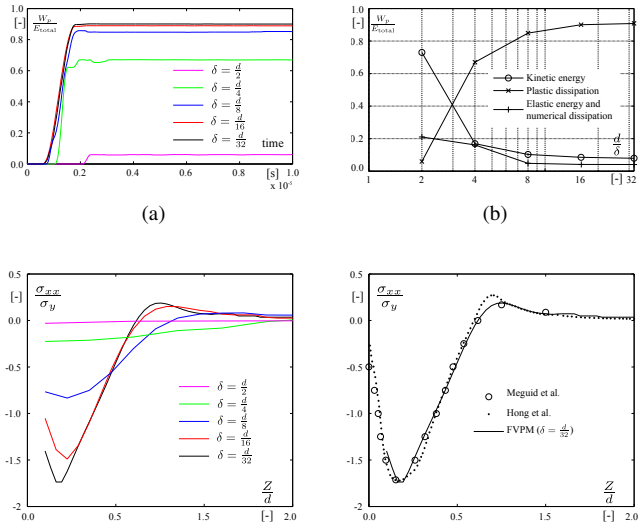

Fig. 6: Results for single shot impact with velocity $|\mathbf{C}| = 75$ m s^{-1}. (a) The time history of energy dissipated in plastic deformation for different particles spacing. (b) The kinetic energy and plastic dissipation after impact for different particle spacing. (c) The variation of residual stress σ_{xx} with depth along the central axis for different particle spacing. (d) The residual stress σ_{xx} is compared with Meguid et al. [5] and Hong et al. [6] results.

Acknowledgment

The research leading to the results published in this paper has received funding from both SCCER SoE, the Swiss Energy Center for Energy Research Supply of Electricity, granted by the Swiss Commission for Technology and Innovation (CTI), and the Ark, the foundation for innovation of Valais Canton, through the Project HydroVS.

The authors would like also to acknowledge the financial support and technical assistance of ALSTOM Power Hydro for the development of the SPHEROS software.

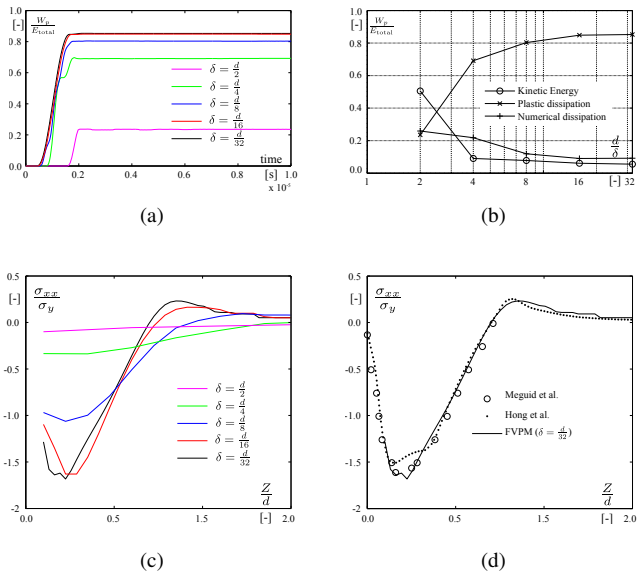

(a) (b) (c) (d)

Fig. 7: Results for single shot impact with velocity $|\mathbf{C}| = 100$ m s^{-1}. (a) The time history of energy dissipated in plastic deformation for different particles spacing. (b) The kinetic energy and plastic dissipation after impact for different particle spacing. (c) The variation of residual stress σ_{xx} with depth along the central axis for different particle spacing. (d) The residual stress σ_{xx} is compared with Meguid et al. [5] and Hong et al. [6] results.

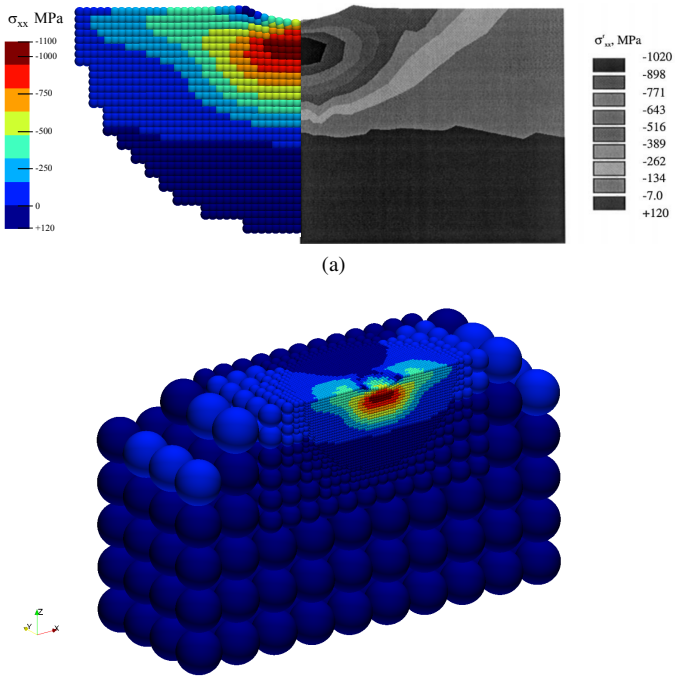

(a) (b)

Fig. 8: Snapshots of solid after shot impact with velocity $|\mathbf{C}| = 75$ m s^{-1} and $\delta = \frac{d}{32}$. (a) residual stress σ_{xx} contours in XZ plane for the present study is shown in left and Meguid et al. [5] solution is shown in right. (b) A 3-D view of solid colored by σ_{xx}. The particles are represented by spheres with radius h and are split near the contact point.

REFERENCES

[1] D. Hietel, K. Steiner, and J. Struckmeier, "A finite-volume particle method for compressible flows," *Mathematical Models and Methods in Applied Sciences*, vol. 10, no. 09, pp. 1363–1382, 2000.

[2] N. J. Quinlan and R. M. Nestor, "Fast exact evaluation of particle interaction vectors in the finite volume particle method," in *Meshfree Methods for Partial Differential Equations V*. Springer Berlin Heidelberg, 2011, pp. 219–234.

[3] E. Jahanbakhsh, "Simulation of silt erosion using particle-based methods," Ph.D. dissertation, École polytechnic fédéral de Lausanne, will be defended on June 2014.

[4] E. Jahanbakhsh, O. Pacot, and F. Avellan, "Implementation of a parallel sph-fpm solver for fluid flows," *Zetta Numerical Simulation for Science and Technology*, vol. 1, no. 1, pp. 16–20, 2012.

[5] S. Meguid, G. Shagal, J. Stranart, and J. Daly, "Three-dimensional dynamic finite element analysis of shot-peening induced residual stresses," *Finite Elements in Analysis and Design*, vol. 31, no. 3, pp. 179 – 191, 1999. [Online]. Available: http://www.sciencedirect.com/science/article/pii/S0168874X98000572

[6] T. Hong, J. Ooi, and B. Shaw, "A numerical study of the residual stress pattern from single shot impacting on a metallic component," *Advances in Engineering Software*, vol. 39, no. 9, pp. 743 – 756, 2008. [Online]. Available: http://www.sciencedirect.com/science/article/pii/S0965997807001809

[7] J. O. Hallquist, *LS-DYNA Theory Manual*. Livermore Software Technology Corporation, 2006.

[8] A. Chrysochoos, O. Maisonneuve, G. Martin, H. Caumon, and J. Chezeaux, "Plastic and dissipated work and stored energy," *Nuclear Engineering and Design*, vol. 114, no. 3, pp. 323 – 333, 1989. [Online]. Available: http://www.sciencedirect.com/science/article/pii/0029549389901106

[9] R. M. Nestor, M. Basa, M. Lastiwka, and N. J. Quinlan, "Extension of the finite volume particle method to viscous flow," *Journal of Computational Physics*, vol. 228, no. 5, pp. 1733–1749, 2009.

[10] G. A. Dilts, "Moving-least-squares-particle hydrodynamicsi. consistency and stability," *International Journal for Numerical Methods in Engineering*, vol. 44, no. 8, pp. 1115–1155, 1999.

[11] J. J. Monaghan, "Smoothed particle hydrodynamics," *Annual review of astronomy and astrophysics*, vol. 30, pp. 543–574, 1992.

[12] M. J. Berger and J. Oliger, "Adaptive mesh refinement for hyperbolic partial differential equations," *Journal of Computational Physics*, vol. 53, no. 3, pp. 484 – 512, 1984. [Online]. Available: http://www.sciencedirect.com/science/article/pii/0021999184900731